Supporting Information:
Thermodynamic Origins of the Interfacial–Bulk Solubility Trade-off for CO_2 in Ionic Liquids: A Molecular Dynamics Simulation Study

Sanchari Bhattacharjee, Shiang-Tai Lin *

Department of Chemical Engineering, National Taiwan University, Taipei, Taiwan 10617

SectionS1: Dimension of Simulation Box used for Bulk ILs Systems

Simulation cell dimensions for 500 ion pairs of [BMIM][BF4] and [BMIM][NTF2]. The table highlights the differences in cell sizes along the x- and y-axes, with [BMIM][BF4] occupying a smaller space (5.39 nm) compared to [BMIM][NTF2] (6.09 nm), reflecting variations in molecular structure and packing density between the two ionic liquids.

Table S1. Dimension of Simulation Box used for Bulk ILs+CO_2 Systems

Simulation setup parameters for CO_2 in ionic liquids [BMIM][BF4] and [BMIM][NTF2] at various temperatures and pressures. The table lists the total gas pressure, simulation box size along the *z*-axis, and the number of CO_2 molecules used in each system.

System	Temperature (K)	Total gas pressure (bar)	Box size along z-axis (nm)	Number of CO_2 molecules
[BMIM][BF4]	303	8	100	1000
[BMIM][BF4]	353	8	137.47	1000
[BMIM][NTF2]	303	8	100	1000
[BMIM][NTF2]	353	8	78.56	700

Section S2. Validation of simulation results for bulk ionic liquid

The experimental values are in great agreement with the calculated densities from the MD simulation; the maximum deviations are 1.00% for [BMIM][BF4] and 0.68% for

[BMIM][NTF2]. The density results imply that the OPLS-AA force-field used for the simulations is reliable/appropriate.

Table S2. Mass Density for ILs for bulk System

ILs	**Density/cm^3**
BMIMBF4	1.198
Experimental	1.21[1]
BMIMNTF2	1.46
Experimental	1.47[2, 3]

Section S3. Molecular mass diffusivity calculation

Diffusion coefficients are obtained by applying Einstein's relation to the linear regions of the calculated mean square displacements (MSDs) [4]. MSDs are calculated using the centre of mass (COM) of the molecules over a 50 ns NVT trajectory and are shown in **Figure S1**. Self-diffusion coefficients of cations and anions for different ILs at 1 bar and 300K.MSDs for calculation of diffusion coefficient are plotted in **Figure S1**. The diffusion coefficient values were derived from the trajectory average of 50 ns of production run. Diffusion constant is computed for its centre of mass of each species. The motion state of gas molecules can be expressed by mean square displacement (MSD), which describes the average distance of all particles from their initial point at time t. MSD can be expressed as the following equation:

$$MSD = \left\langle \left| \vec{r}_i(t) - \vec{r}_i(0) \right|^2 \right\rangle \quad \textbf{(S1)}$$

Where $\vec{r}_i(t)\ and \vec{r}_i(0)$ represent the position vector of the atom at time t and time 0, respectively. < > represent the average of all particles in the model. The diffusion coefficient can be derived from Equation (S2)[5].

$$D = \frac{\left|\vec{r}_i(t) - \vec{r}_i(0)\right|^2}{6t} = \frac{a}{6}$$ **(S2)** where a is the slope of the curve fitted by MSD

Figure S1. shows the self-diffusion coefficients of cations, anions, and CO_2 in different ionic liquids at 1 bar and 300 K. In both systems, the ionic species exhibit much lower diffusivities than CO_2, with cation and anion diffusivities on the order of 10^{-12}–10^{-11} m^2/s, while CO_2 diffusivities are approximately 10^{-10} m^2/s. This indicates that CO_2 is significantly more mobile than the ionic components, which is expected because CO_2 is a small, neutral molecule that experiences fewer electrostatic interactions and less steric hindrance within the ionic liquid environment. Comparing the two ionic liquids, the BMIM cation exhibits higher diffusivity in [BMIM][NTF2] than in [BMIM][BF4]**,** indicating greater ionic mobility in the NTF_2-based system. This trend is consistent for both cations and anions and suggests that [BMIM][NTF_2] has lower viscosity and weaker ion–ion interactions than [BMIM][BF4], resulting in enhanced molecular mobility.

Table S3. Experimental and simulated diffusivities (in m^2/s) of the cation, anion, and CO_2 in ILs at at T =300 K, $P \approx 1$ bar, and specified CO_2 mole fractions

[BMIM][BF4] Diffusivity (m^2/s)	Cation	Anion	CO_2
Experimental	10.01×10^{-12} [1, 6]	6.67×10^{-12} [1, 6]	3×10^{-10} [1, 6] for $x_{CO_2} = 0.016$
Simulated	9.57×10^{-14}	7.21×10^{-14}	1.25×10^{-11} for $x_{CO_2} = 0.029$
[BMIM][NTF2] Diffusivity (m^2/s)	2.4×10^{-11} [7]	2.0×10^{-11} [7]	
Experimental	24.14×10^{-12} [8]	21.07×10^{-12} [8]	
	1.74×10^{-11} [9]	1.03×10^{-11} [9]	

			1.9×10^{-10} ^{10} for $x_{CO_2} = 0.029$
Simulated	3.538×10^{-13}	2.76×10^{-13}	2.21×10^{-11}

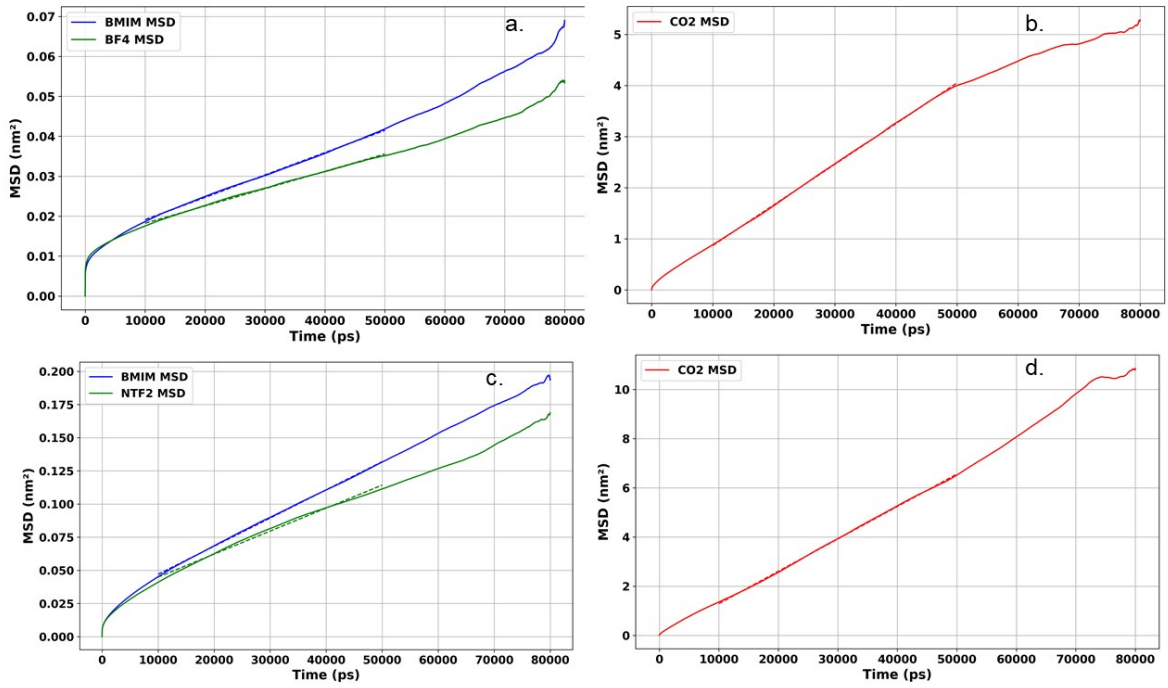

Figure S1. MSD plots of ILS of CO_2/IL bulk systems a) MSDs for Cation and Anion of [BMIM][BF4] b) CO_2 of [BMIM][BF4] d) MSDs for Cation and Anion of [BMIM][NTF2] b) CO_2 of [BMIM][NTF2]. Standard deviation in diffusion coefficient was less than 5% in all the cases.

S4. Viscosity calculation

For each ionic liquid (IL), the shear viscosity is calculated using the Green-Kubo equation [11, 12] which integrates the pressure tensor autocorrelation function over time. The equation is as follows:

$$\eta = \frac{V}{k_B T} \lim_{t \to \infty} \int_0^t \langle P_{\alpha\beta}(0) P_{\alpha\beta}(t) \rangle dt \qquad \textbf{(S3)}$$

V represents the system volume, T is the temperature, k_B is the Boltzmann constant, $P_{\alpha\beta}$ are the components of pressure tensor ,with $\alpha,\beta = x,y,z,$To ensure more reliable results, viscosity is calculated by averaging three independent pressure tensor components: $P_{xy,}P_{yz,}$ and P_{xz}. The calculation is carried out in the canonical ensemble (NVT) because the Green-Kubo equation is defined for systems with constant volume. Equilibrium molecular dynamics (MD) simulations were performed using the LAMMPS software package[13]. The CL&Pol force field [14]was employed to describe both inter- and intramolecular interactions of the ionic liquid (IL) molecules[15]algorithm with a real-space cut-off of 12 Å. Lennard–Jones interactions were also truncated at 12 Å, and periodic boundary conditions were applied in all three spatial directions. A time step of 1 fs was used for all simulations. Initial configurations were generated using the Packmol package [16]by randomly placing 280 IL molecules in a cubic simulation box. The system was first equilibrated for 2 ns in the isothermal–isobaric (NPT) ensemble at 300 K and 1 atm, followed by production simulations in the canonical (NVT) ensemble. Shear viscosity was calculated using the Green–Kubo formalism[17]. The off-diagonal components of the pressure tensor were sampled every 2 fs over a correlation length of 100 ps. The corresponding autocorrelation functions were integrated using the trapezoidal rule, and the final viscosity was obtained as the average of the three independent components.

Table S4. Comparison of viscosity for [BMIM][BF4] and [BMIM][NTF2] at 300 K from experimental studies, previous computational results, and the present study.

ILs	Viscosity(Cp)		
	Experimental	Computational	Our Study
BMIMBF4	94.26[18] 109.8[19]	95 [1] 98.5[19]	110.24
BMIMNTF2	50 [20] 51.2 [19]	58.5 [19]	50.29

S5. Vapour–Liquid Equilibrium and Critical Parameters of Pure CO_2

Table S5. Comparison of CO_2 critical properties from selected simulation studies

(Potoff and Siepmann, 2001)[21]	Tcritical 306.2 K ρcritical 0.4649 g/ml
(Eggimann et al., 2019)[22]	Tcritical 303.75 K ρcritical 0.5073 g/ml Pcritical 7.84 MPa
(Hong et al., 2024)[23]	Tcritical 304.13 K, Pcritical 7.38 MPa

This discrepancy can be attributed to differences in the force field parameters used for CO_2. In our simulations, we employed a rigid linear triatomic model for CO_2 from the work of Shi and Maginn[24], and which has been validated for CO_2 solubility/thermodynamics in lmidazolium [NTF2] ILs[24-26]. Using the rigid variant preserves the validated non-bonded interactions while improving numerical stability and sampling efficiency for large interfacial systems[27, 28].

Further, the vapour pressure (P^{vap}) of CO_2 was determined from simulation at temperatures below the estimated critical temperature. In our simulations, vapour pressures were calculated at 273, 283, 293, 298, and 300 K, with values ranging from –0.20 bar (273 K) to 21.41 bar (300 K). For temperatures at or above the estimated Tc (317.9 K), the system becomes supercritical, and vapour pressure is not defined **(Figure S2).** Vapour–liquid equilibrium (VLE) analysis was performed only up to 300 K, below the simulated critical temperature (Tc ≈ 318 K for our model). Above Tc, the distinction between liquid and vapour phases disappears, as the density difference vanishes and the interface becomes ill-defined.

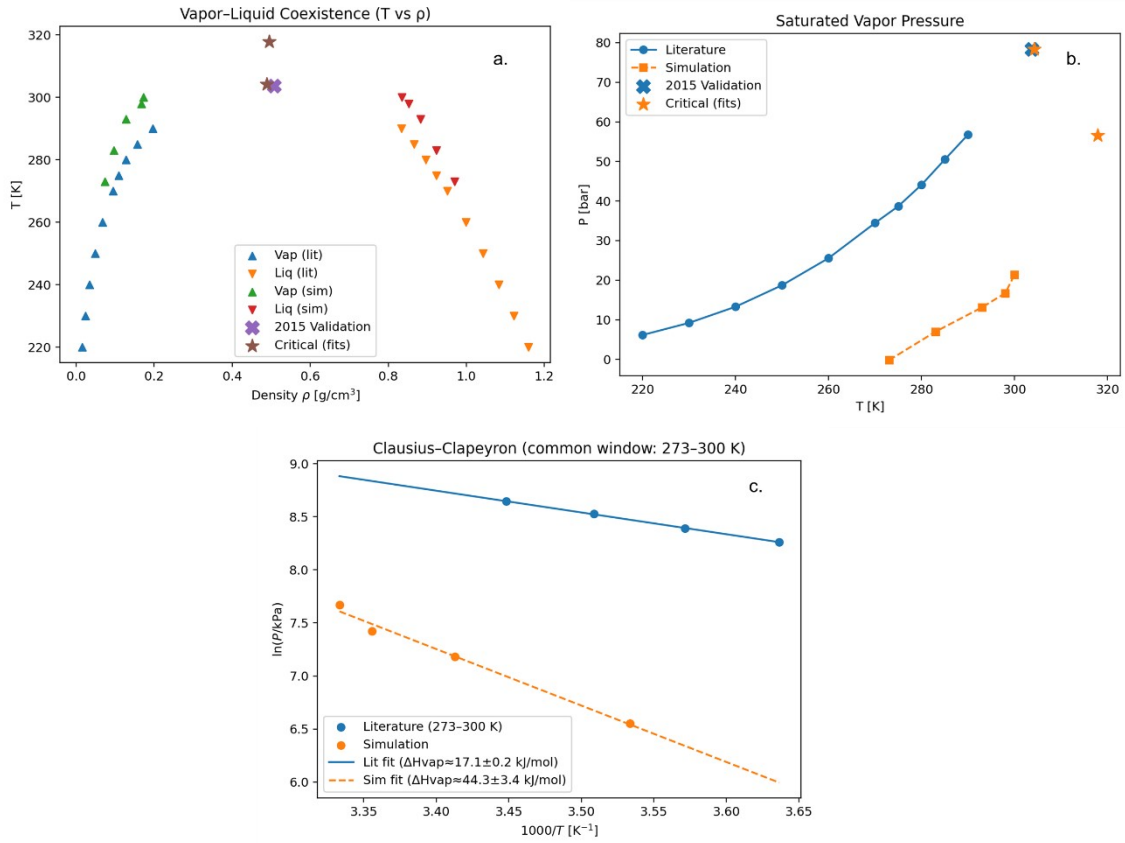

Figure S2. *(a)* Vapour–liquid coexistence curve (T vs. density) for pure CO_2: simulation results (green/red) and literature data (blue/orange). The critical point from simulation (star) and experimental validation (cross) are shown for comparison.*(b)* Saturated vapour pressure curves for CO_2, with simulation (orange) and literature (blue) data, along with critical point estimates.

(c) Clausius–Clapeyron analysis (ln P vs. 1/T) restricted to the 273–300 K window where both simulation and experiment yield stable vapour–liquid equilibrium. The enthalpy of vaporization (ΔHvap) is obtained from the slope, but not extrapolated above 300 K, where the simulation no longer maintains two-phase coexistence. From literature[22] , the critical temperature (Tc) of CO_2 is 303.75 K, the critical density (ρc) is 0.5073 g/mL, and the critical pressure (Pc) is 78.4 bar. The simulated vapour pressures as a function of temperature are summarized in **Figure S2. (right panel),** where the natural logarithm of the vapour pressure is plotted versus inverse temperature in accordance with the Clausius–Clapeyron relation. The critical temperature (Tc) and critical density (ρc) were estimated by simultaneous least-squares fits to the rectilinear diameter law and order parameter scaling law using all

subcritical coexistence points, with the universal critical exponent (β=0.326). The critical pressure (Pc) was estimated by polynomial extrapolation of the saturated vapour pressure curve to Tc.

These expressions are derived from the integrated Clausius–Clapeyron equation:

$$\ln P = -\Delta Hvap / (R\ T) + C \qquad \textbf{(S4)}$$

where ΔHvap is the enthalpy of vaporization, R is the universal gas constant, and C is a constant.

S6. Identifying Interface, Bulk and vapour Regions

To locate vapour, bulk, and interfacial regions, the two broad CO_2 maxima and their neighbouring minima were identified; the flat central section between the minima was taken as the bulk region, and the low-density zones near the box edges as vapour. Interfacial adsorption was then quantified using geometrically defined slabs. A bulk IL density was obtained from the plateau of the IL profile, and side-specific CO_2 vapour baselines were determined from the vapour windows. On each side, the inner interfacial boundary was set at the first position (moving from vapour toward the centre) where the IL density reached its bulk value, and the outer boundary at the position beyond the CO_2 peak where the CO_2 density dropped to within 5% of its vapour baseline. These bounds define the left and right interfacial windows used for analysis. All quantitative values reported in **Tables 1–S6.** (counts, CO_2/IL ratios, enrichment E, bulk mole fraction $x CO_2$, interfacial thickness, were obtained from molecular centre-of-mass **(COM)** density profiles.

To quantify interfacial adsorption, we used geometrically defined interfacial windows. First, a bulk IL region was identified from the flat portion of the IL density plateau, and separate vapour windows were used to determine side-specific CO_2 vapour baselines. The inner boundary of the interfacial slab on each side was placed at the first position, moving towards bulk IL where the IL density profile crossed the horizontal line corresponding to 100% of this bulk IL density. The outer, vapour-side boundary was determined from the CO_2 profile: on each side we located the interfacial CO_2 peak, defined a peak-relative threshold a small fraction (5%) above the vapour baseline, and moved outward from the peak toward the

vapour until the CO_2 density first fell below this threshold. These two points – the IL-bulk crossing on the liquid side and the threshold-based CO_2 crossing on the vapour side – define the left and right interface windows used in the analysis. The interfacial thickness reported in the manuscript is the average of the widths of these left and right windows. Gibbs dividing surface (GDS)it is computed solely as a diagnostic check to verify that the density profiles behave normally and that the system contains a well-formed liquid–vapour interface

Finding the Gibbs Dividing Surface: For each side (left/right), the code finds the **z_0 position** where the area (integral) of the "excess" density (above vapour) on one side equals the "deficit" (below bulk) on the other side.

Profiles. We define the total ionic number-density profile as

$$\rho_{IL}(z) = \rho_{cation}(z) + \rho_{anion}(z) \quad \text{(S5)}$$

To stabilize the construction of the dividing surfaces we smooth $\rho_{IL}(z)$ with a Savitzky–Golay filter (odd window, polyorder 3); all integrals are evaluated on the original grid using linear interpolation at segment boundaries.

Baselines. The bulk IL baseline ρℓ is the mean of $\rho_{IL}(z)$ over a narrow central "plateau" window $[z_l^{min}$ and $z_l^{max}]$,The vapour baselines on the left/right, ρ_v^L and ρ_v^R are the means of $\rho_{IL}(z)$ over low-density edge windows$[z_v^{L,min}, z_v^{L,max}]$ and $[z_v^{R,min}, z_v^{R,max}]$ respectively.

Gibbs dividing surfaces (equal-area conditions).

Let z_{min} and z_{max} denote the ends of profile z-domain, and let z_{mid} be the midpoint of the bulk window. The left and right dividing surfaces, z_0^L and z_0^R ,satisfy

$$\int_{z_{min}}^{z_0^L} [\rho_{IL}(z) - \rho_v]dz = \int_{z_0^L}^{z_{mid}} [\rho_l - \rho_{IL}(z)]dz \quad \text{(S6)}$$

$$\int_{z_{min}}^{z_0^R} [\rho_{IL}(z) - \rho_l]dz = \int_{z_0^R}^{z_{mid}} [\rho_v^R - \rho_{IL}(z)]dz \quad \text{(S7)}$$

(These equations are solved numerically with Brent's method on bracketing intervals around each interface.)

S.7 Calculation of Interfacial Properties

Density Profiles and Regions

Cross-sectional Area and Total Box Volume

- **Cross-sectional area (nm²):**
  The area of the simulation box in the x-y plane:

A=$L_x \times L_y$,where L_x and L_y are the box lengths in x and y, V=A($z_{max} - z_{max}$)

CO_2 in interfacial Region. The number of CO_2 molecules in GDS slab is

$$N_{CO_2}^{interface} = A \int_{z_0^{left}}^{z_0^{right}} \rho co_2(z) dz \ldots$$ **…….(S8)**

The solubility is represented as the mole fraction of CO_2 absorbed in the IL and calculated using the following expression:

$$x_{CO_2} = \frac{Nco_2{}^{bulk}}{Nco_2{}^{bulk} + N_{IL}{}^{bulk}}$$ ……. **(S9)**

$Nco_2{}^{bulk}$=Total no. of CO_2 molecules in bulk region, and

$$N_{IL}{}^{bulk} = \frac{N_{cation}{}^{bulk} + N_{anion}{}^{bulk}}{2}$$ ……. **(S10)**

To quantify the relative accumulation of CO_2 at the interface, we define the enrichment factor

E = $(NCO_2/NIL)_{interface} / (NCO_2/NIL)_{bulk}$

For each region, the effective number of molecules is obtained from the density profile by integrating over the corresponding z-window,

$$N_{species} = \int_{za}^{zb} \rho_{species}(z) dz,$$ ……(S11)

where $N_{species}$has units of molecules per unit cross-sectional area (molecules/nm²). Dividing by the region width Δz=zb−za gives the average three-dimensional number density in that region,

$$\rho_{species} = \frac{N_{species}}{\Delta z} \quad \text{..... (S12)}$$

Substituting into Eq. (S11) gives the final form used in the analysis:

$$E = \frac{\rho avgCO_2,interface/\rho ILavg,interface}{\rho avgCO_2,bulk/\rho ILavg,bulk} \quad \text{.....(S13)}$$

Because E is written entirely in terms of average densities, any dependence on the cross-sectional area or on the absolute number of molecules cancels out. Thus, E is a robust, dimensionless measure of interfacial enrichment that is directly comparable across simulations with different system sizes or compositions.

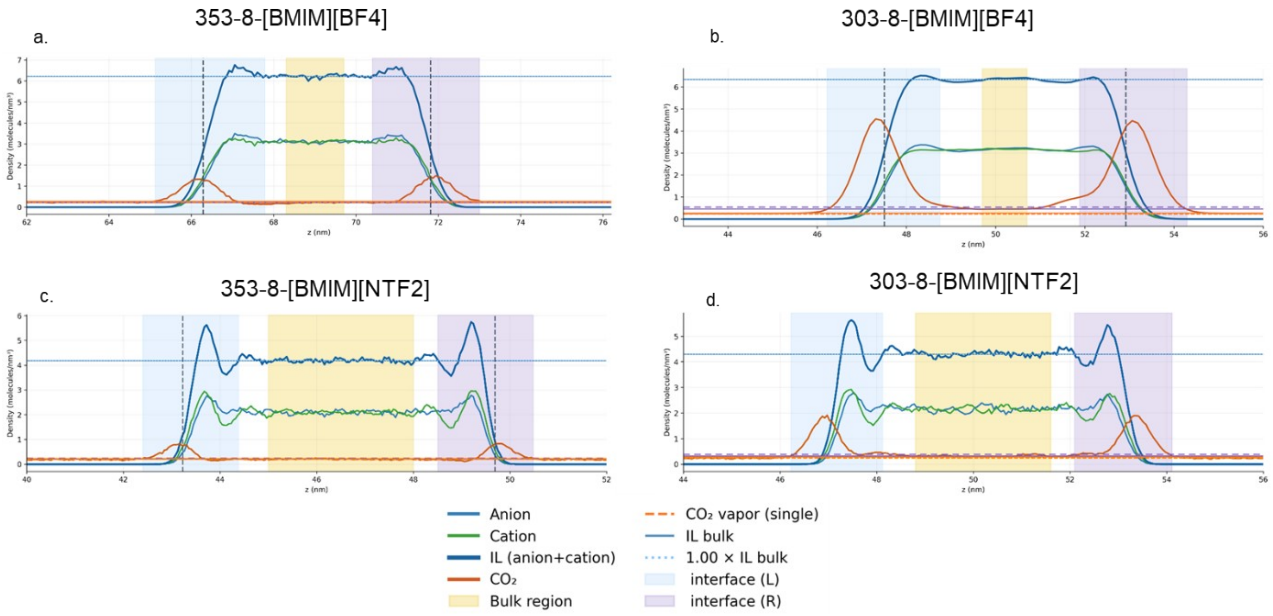

Figure S3. Number-density profiles of the anion, cation, total ionic liquid (IL), and CO_2 along the surface normal z. The yellow shading denotes the IL bulk region, defined as the

central plateau where the IL density is constant. The blue and purple shadings mark the left and right interfacial windows, respectively, bounded by the positions where the IL density first falls below 1.00×ρIL, bulk and where the CO_2 density returns to its vapour-side baseline. The horizontal blue dotted line indicates the bulk IL density, and the vertical dashed lines show the locations of the Gibbs dividing surface (GDS) The orange dashed curve shows the low CO_2 vapour density at the box edges.

Table S6. Distribution of CO_2 at the Interface and Bulk Region in Different ILs under Various Conditions

Property	303-8-[BMIM][NTF2]	303-8-[BMIM[[BF4]	353-8-[BMIM][BF4]	353-8-[BMIM][NTF2]
Interfacial thickness (nm)	1.9585	2.47395	2.63100215	1.9756165
CO_2 in Bulk Region (molecules)	32.8819871	13.18319962	8.648373404	22.61418576
IL in Bulk Region (molecules)	222.6430778	92.80184949	126.5494205	232.229914
CO_2 in Interface Region (molecules)	129.1280654	329.1968321	104.6827393	57.38321526
IL in Interface Region (molecules)	181.4538729	213.0183453	263.1362621	178.3569177
First Peak CO_2/area (molecules/nm^2)	1.680728266	5.680127628	1.744865293	0.786129525
Second Peak CO2/area (molecules/nm^2)	1.807043144	5.651130083	1.858410867	0.763801057
First Peak IL/area	4.715325505	7.976611272	9.329841774	4.770284307

(molecules/nm^2)				
Second Peak IL/area (molecules/nm^2)	5.086875557	6.687963428	8.784942497	4.864618161
E	4.8176276	10.75628988	5.800846894	3.305567432

S8. Radial distribution function calculation and coordination number

Two–dimensional (in–plane) radial distribution functions, $g_{xy}(r)$, were computed with GROMACS using the gmx rdf module with the -xy option. In this mode, intermolecular distances are evaluated in the plane parallel to the interface, i.e. using the projected separation

$r=\sqrt{(xi-xj)^2+(yi-yj)^2}$, **……..(S14)** ,while the z–coordinate is used only to select molecules within a given slab.

Molecules were selected on the basis of their centre–of–mass (COM) positions using selections of the form:

$z_{low} \leq z < z_{high,}$…… **(S15)**

thereby restricting both reference and neighbour molecules to a specified interfacial region (first peak, bulk-like layer, or second peak).

For each region and each pair of species A and B, the in–plane RDF was obtained with a command of the form:

```
gmx rdf -xy \
    -selrpos whole_mol_com -seltype whole_mol_com \
    -ref "resname A and z >= Z_low and z < Z_high" \
    -sel "resname B and z >= Z_low and z < Z_high" \
    -bin 0.05 -rmax 2.5 ……(S16),
```

where -bin and -rmax set the radial bin width and maximum distance, respectively.

The 3D radial distribution functions (RDFs), $g_{ij}(r)$, and corresponding coordination numbers, n_{coord}, are calculated using Equations S14-15.

$$g_{ij}(r) = \frac{\langle n_{ij}(r) \rangle}{4\pi r^2 \rho_{j\,dr}} \qquad \ldots\ldots\ldots\ldots\ldots\ldots \textbf{(S17)}$$

$$n_{coord} = 4\pi\rho_{j} \int_{0}^{rmin} g_{ij}(r)\, r^2 dr \qquad \ldots\ldots\ldots \textbf{(S18)}$$

where $\langle n_{ij}(r) \rangle$ is the ensemble average of the total number of jth type particles in the small volume element $4\pi r2\ dr$ at a distance r from the central ith-type particle. $\rho_i$is the bulk number density of jth-type particles. Here, $rmin$ refers to the positions of the first minimum of the RDFs

Two types of 2D RDFs were evaluated in **Figure S5**. (i) full-plane RDFs over the entire box (no z-filter), and (ii) slab RDFs, where the simulation box was partitioned into non-overlapping slabs of thickness Δz = 1.0 nm along z, and g(r) was computed independently in each slab for the same set of pairs (BMI–anion, anion–CO_2, BMI–CO_2, CO_2–CO_2). The slab RDFs were then averaged over all slabs to give a single curve per pair and thickness. As a consistency check, we also calculated conventional 3D COM–COM RDFs for the full box.

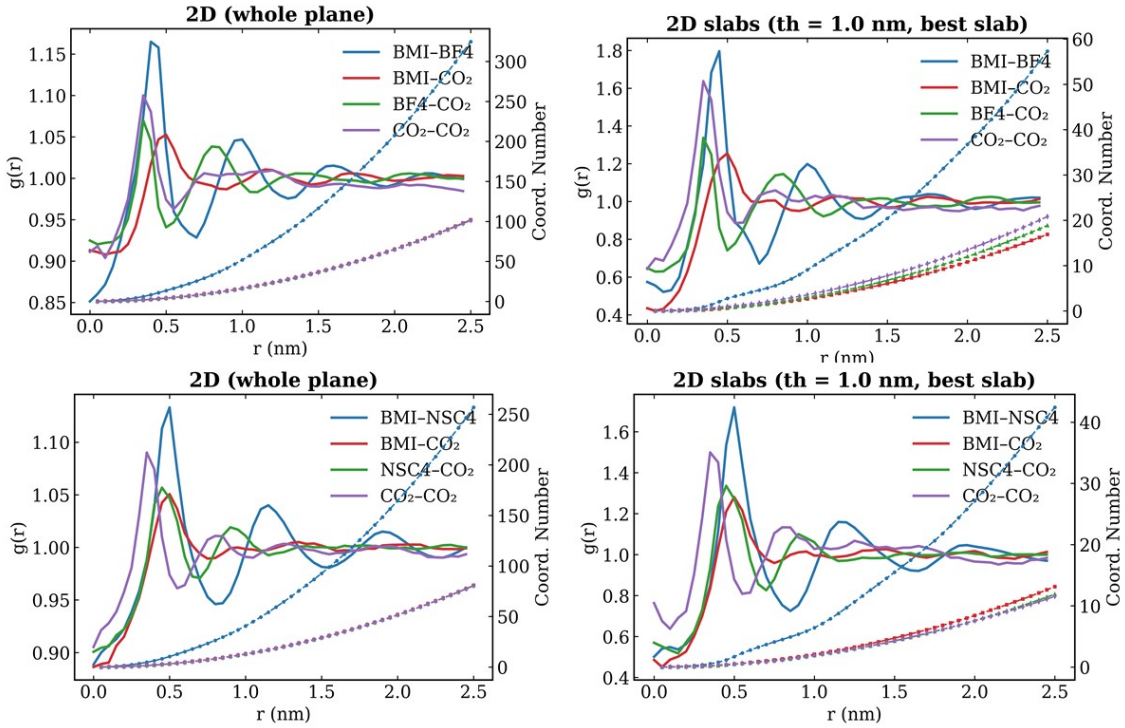

Figure S4. 2D–XY centre-of-mass RDFs g(r) (solid lines) and cumulative coordination numbers N(r) (dashed lines) for homogeneous [BMIM][BF4]–CO_2 (top) and [BMIM][NTF2]–CO_2 (bottom) mixtures. Left panels: RDFs evaluated over the full simulation plane (no z-filter). Right panels: RDFs averaged over central slabs of thickness Δz = 1.0 nm, matching the slab thickness used in the interfacial analysis. The close agreement between full-plane and slab-averaged curves, and the approach of g(r) → 1 at large r, confirm that these homogeneous simulations provide a valid bulk reference for comparison with the interfacial systems.

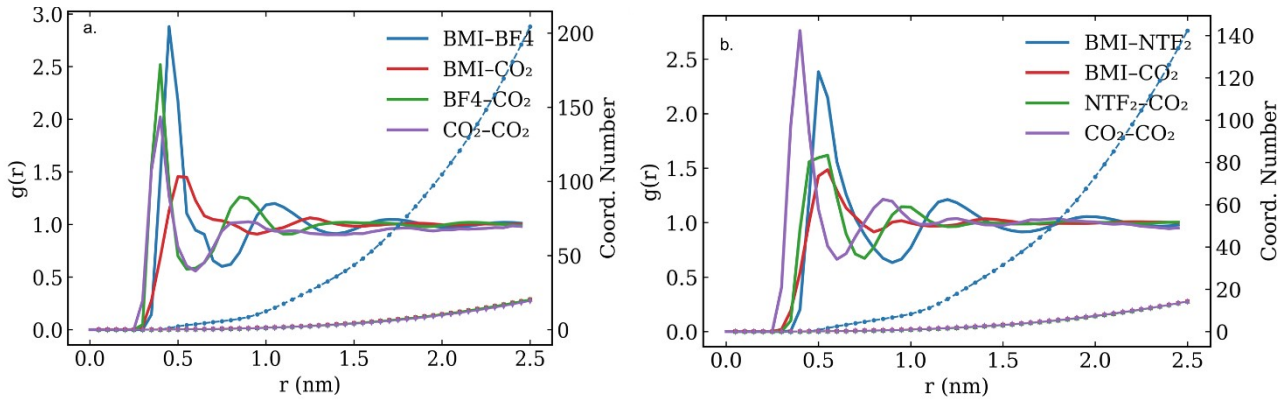

Figure S5. Centre of RDF g(r) between the (a) [BMIM][BF4] and (b) [BMIM][NTF2] at T = 300 K and P = 1 bar

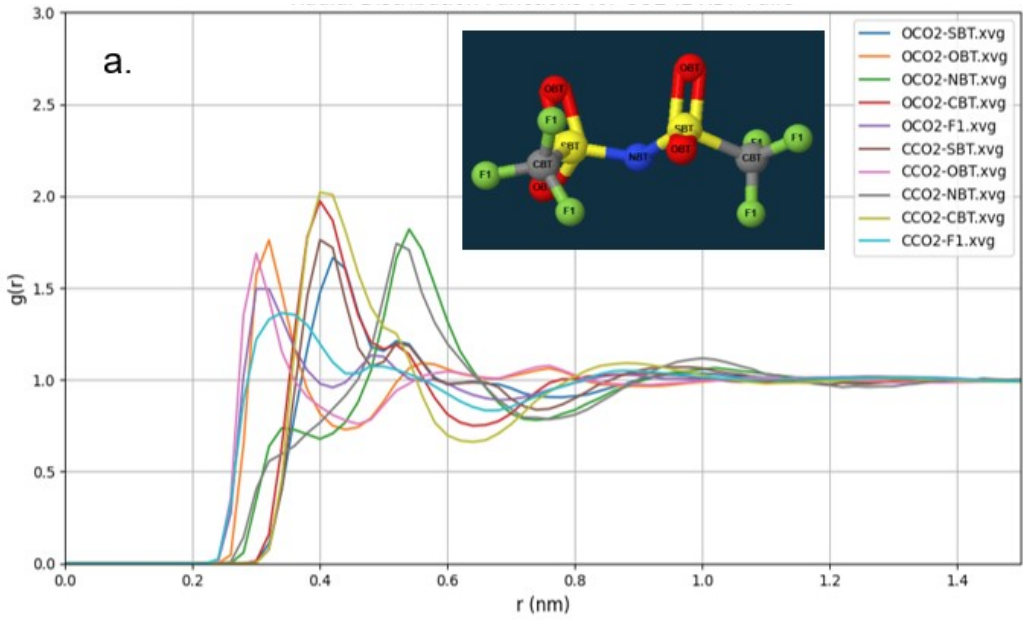

Figure S6.RDF plots between each atom of a) [NTF2]and CCO_2 and OCO_2

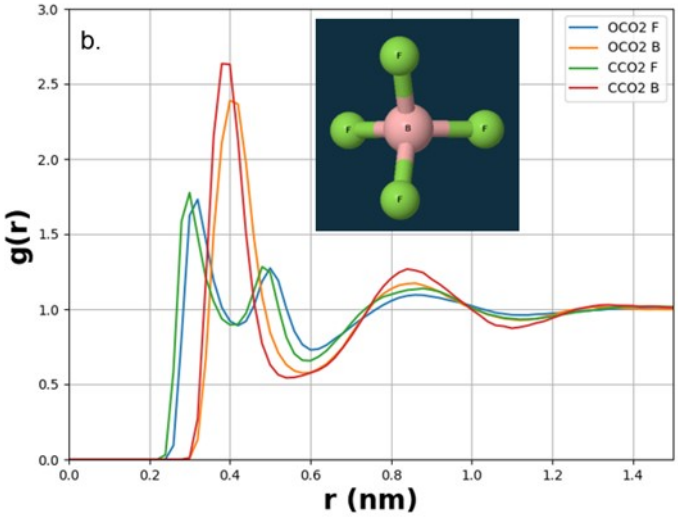

Figure S7.RDF plots between each atom of b) [BF4]and CCO_2 and OCO_2

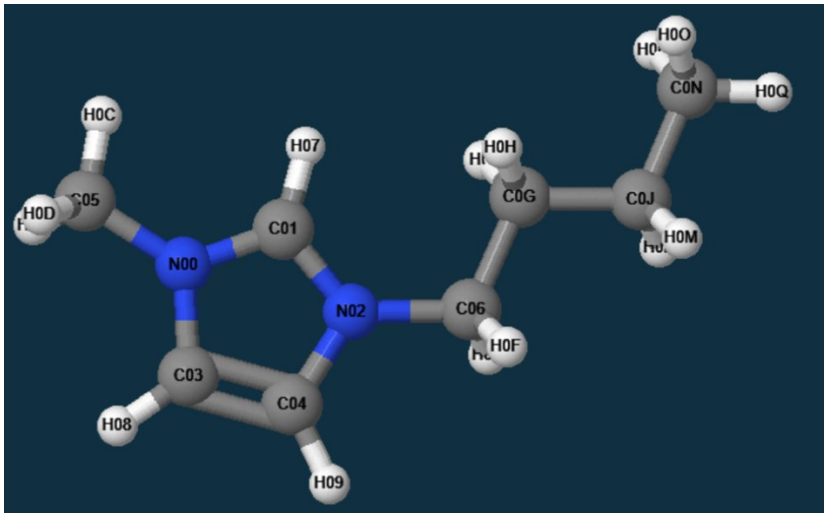

Figure S8. The atomic label of [BMIM] for RDFs and Coordination Number Calculation

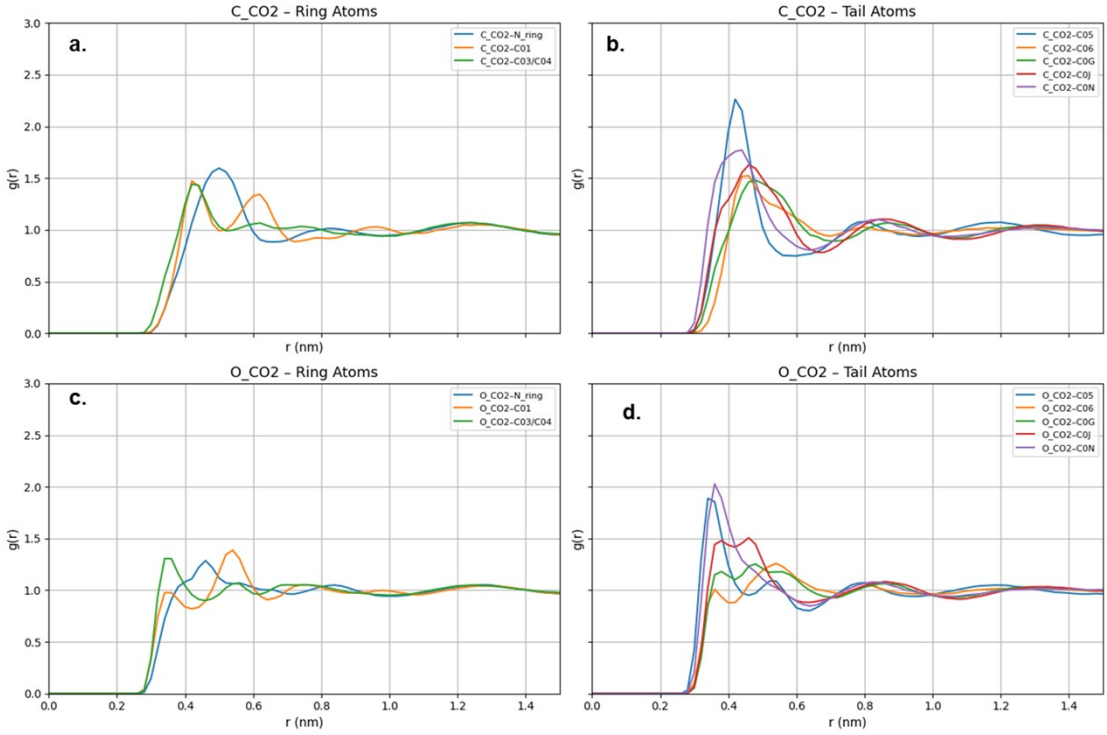

FigureS9. RDF plots between each atom of [BMIM] and CCO_2 and OCO_2 (a)-(d) [BMIM][BF4]

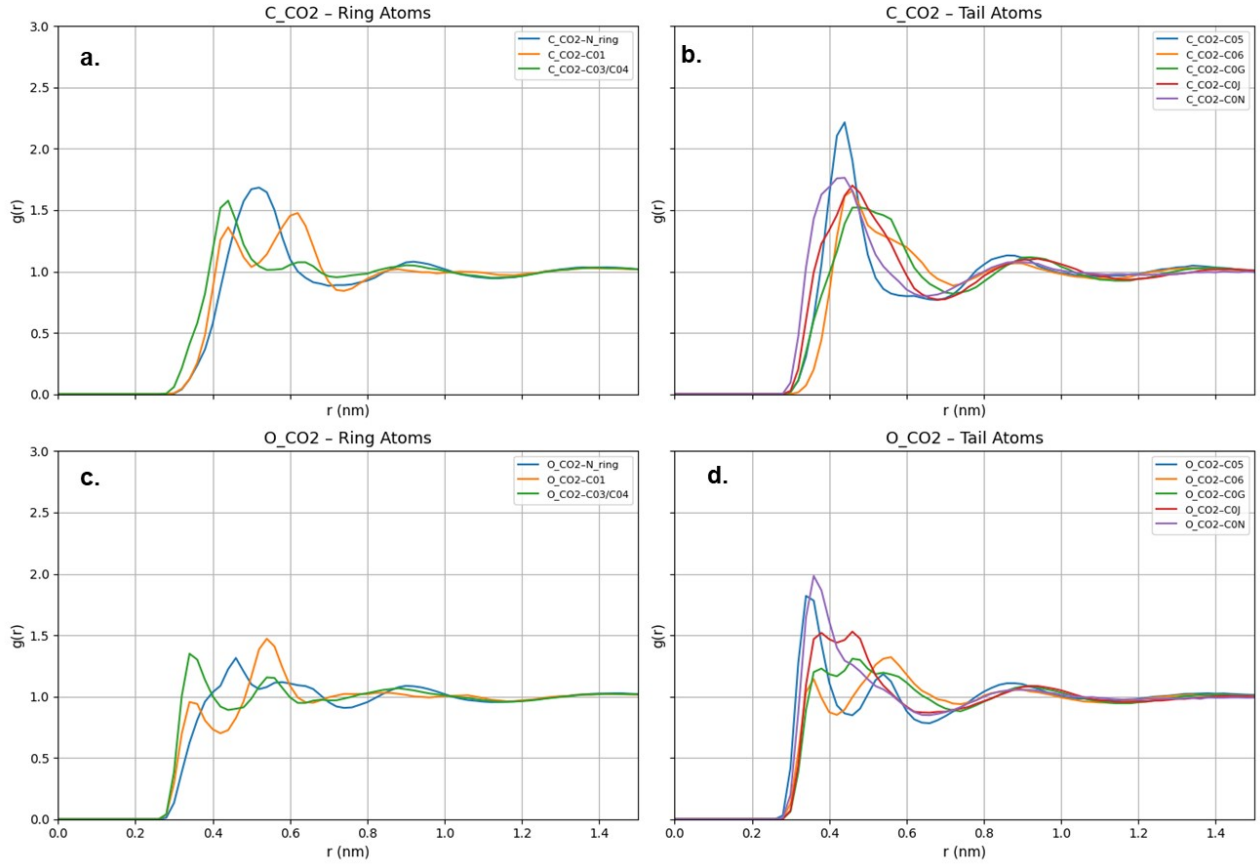

FigureS10. RDF plots between each atom of [BMIM] and CCO_2 and OCO_2 (a)-(d) [BMIM][NTF2]

Table S7. Coordination number of COM RDFs between BMIM, Anion and CO_2

RDF Pairs	Rmin	Coordination No.
BMI-BF4	0.76	5.633
BMI-CO_2	0.934	0.997
BF4-CO_2	0.56	0.206
BMI-NTF2	0.9	6.332
BMI-CO_2	0.81	0.471

NTF2-CO_2	0.73	0.351

TableS8. Coordination number of atom-atom RDFs between BMIM and CO_2

RDF	Coordination No.[BMIM][BF4]	Rmin[BMIM][BF4]	Coordination No.[BMIM][NTF2]	Rmin[BMIM][NTF2]
CCO_2-Nring.	0.340214	0.66	0.310906	0.71
CCO_2-C01	0.487204	0.74	0.346407	0.74
CCO_2-C03-C04	0.156775	0.53	0.143527	0.57
CCO_2-C05	0.26052	0.6	0.24568	0.68
CCO_2-C06	0.403831	0.7	0.315527	0.72
CCO_2-C0G	0.415781	0.7	0.319463	0.72
CCO_2-C0J	0.388432	0.68	0.2743	0.68
CCO_2-C0N	0.329991	0.64	0.231274	0.64
OCO_2-Nring	0.465703	0.74	0.355996	0.744
OCO_2-C01	0.323991	0.65	0.227127	0.65
OCO_2-C03-C04	0.082004	0.45	0.056832	0.45
OCO_2-C05	0.104898	0.46	0.077615	0.465
OCO_2-C06	0.47526	0.74	0.363715	0.755
OCO_2-C0G	0.478952	0.74	0.363686	0.755
OCO_2-C0J	0.345002	0.647	0.226156	0.631
OCO_2-C0N	0.349981	0.658	0.245945	0.653

TableS9. Coordination number of RDFs between NTF2 and BF4 and CO_2

RDF	Coordination number	R_{min}
OCO_2-SBT	0.418	0.79
OCO_2-OBT	0.056	0.44
OCO_2-NBT	0.347	0.74
OCO_2-CBT	0.221	0.64
OCO_2-F1	0.059	0.428
CCO_2-SBT.	0.355	0.75

CCO_2-OBT.	0.065	0.46
CCO_2-NBT.	0.366	0.76
CCO_2-CBT	0.222	0.64
CCO_2-F1	0.233	0.66
CCO_2-F	0.24	0.6
CCO_2-B	0.2	0.54
OCO_2-F	0.24	0.6
OCO_2-B	0.23	0.58

Table S10. Molar Volumes of ILs Systems with and without CO_2 at 300K

System	Molar Volume cm^3/mol
[BMIM][BF4]	189.17
[BMIM]BF4]+CO_2	174.687
[BMIM][NTF2]	271.69
[BMIM[NTF2]+CO_2	250.96

The values suggest that [BMIM][BF4] is more tightly packed compared to [BMIM][NTF2], as reflected by its lower molar volume. When CO_2 is introduced, the volume slightly decreases, which could indicate that CO_2 molecules are filling voids between the ionic liquid molecules. The decrease in molar volume when CO_2 is added points to CO_2 fitting into the ionic liquid structure and potentially forming a more compact arrangement or interactions between CO_2 and the IL molecules. The magnitude of this change is small, suggesting that CO_2 does not drastically alter the overall packing structure but may slightly reduce the free volume. [BMIM][NTF2] has a larger molar volume than [BMIM][BF4], which is consistent with its larger anion [NTF2] compared to the BF4 anion in [BMIM][BF4].

Table S11. Comparison of average fractional free volume (FFV) and average free volume (nm^3) for [BMIM][BF4] at various probe radii, evaluated for systems with and without dissolved CO_2

Probe Radius (nm)	Avg FFV% (No CO_2)	Avg FFV% (With CO_2)	Avg FreeVol (No CO_2)	Avg FreeVol (With

			(nm^3)	CO_2)(nm^3)
0.01	29.407	29.362	46.290	46.980
0.02	21.917	21.865	34.499	34.985
0.03	15.505	15.446	24.4064	24.715
0.04	10.403	10.319	16.376	16.511
0.05	6.5813	6.517	10.360	10.428
0.06	3.9487	3.886	6.216	6.218
0.07	2.236	2.182	3.518	3.492
0.08	1.198	1.161	1.887	1.858
0.09	0.609	0.585	0.9587	0.936
0.11	0.136	0.127	0.2145	0.204
0.12	0.059	0.0545	0.0936	0.0873
0.13	0.024	0.0222	0.0389	0.035
0.14	0.009	0.0085	0.0155	0.0137
0.15	0.0038	0.0031	0.006	0.004

Table S12. Comparison of average fractional free volume (FFV) and average free volume (nm^3) for [BMIM][NTF2] at various probe radii, evaluated for systems with and without dissolved CO_2

Probe Radius (nm)	Avg FFV% (No CO_2)	Avg FFV% (With CO_2)	Avg FreeVol (No CO_2) (nm^3)	Avg FreeVol (With CO_2)(nm^3)
0.01	26.620	26.955	60.147	61.885
0.02	19.412	19.752	43.861	45.349
0.03	13.409	13.708	30.297	31.472
0.04	8.734	9.0053	19.735	20.675
0.05	5.377	5.597	12.149	12.85
0.06	3.115	3.274	7.0403	7.517
0.07	1.702	1.812	3.846	4.161
0.08	0.874	0.946	1.976	2.173
0.09	0.427	0.4689	0.966	1.076

0.11	0.086	0.0985	0.1952	0.226
0.12	0.035	0.0426	0.080	0.096
0.13	0.014	0.0167	0.031	0.038
0.14	0.005	0.0067	0.012	0.015
0.15	0.001	0.0024	0.004	0.005

Table S13. Box volumes and the side lengths of Simulation Box

System	Avg. Volume (nm^3)
$BMIMNTF_2$+CO_2	229.6
$BMIMNTF_2$	225.949
$BMIMBF_4$+CO_2	160
$BMIMBF_4$	157.422

S8. Heat Capacity

The isobaric heat capacity (C_p) of each ionic liquid (IL) system, with and without CO_2, was determined by performing equilibrium molecular dynamics simulations at multiple temperatures in the NPT ensemble. Simulations were carried out over the temperature range of 288.15–353.15 K. At each temperature, the time-averaged values of all relevant energy components—including bond, angle, dihedral, van der Waals (LJ), dispersion correction, Columbic (real and reciprocal), and kinetic energy—were extracted.

The total enthalpy at each temperature was estimated using:

$$H(T) = E\_total + pV \quad \textbf{(S19)}$$

where E_total is the sum of potential and kinetic energy, and pV is the pressure-volume contribution. The heat capacity was calculated as the slope of the enthalpy with respect to temperature:

$C_p = (dH/dT)p$ **(S20)**

For additional insight, the partial contributions to C_p were computed for each individual energy component by performing a linear regression of the component energy vs. temperature data (i.e., $C_p^i = dE^i/dT$). The quality of each linear fit was assessed using the coefficient of determination (R^2), and only components with satisfactory fits were included in the total C_p estimate.

TableS14. Cp Contribution in [BMIM][BF4] vs. [BMIM][NTf2]

Energy Component	[BMIM][BF4] (kJ/mol·K)	[BMIM][NTf2] (kJ/mol·K)
Bond	29.3917	50.1843
Angle	77.7240	111.3343
FourierDih.	21.5815	14.2803
Evdw	34.1317	66.7250
Ecolomb	35.2827	59.1550
Kinetic	155.8782	218.2320
Total Cp	353.9898	519.9196
TotalEnergy	353.9882	519.910
pV	0.0053	0.008652
Total + pV	353.9934	519.9196

TableS15. Cp Contribution in [BMIM][BF4] + CO_2 and [BMIM][NTF2] + CO_2

Energy Component	[BMIM][BF4] + CO_2 (Cp)	[BMIM][NTF2] + CO_2

	[kJ/(mol·K)]	(Cp) [kJ/(mol·K)]
Bond	29.0675	50.0263
Angle	77.3744	111.1144
FourierDih.	22.1534	16.7980
Evdw	39.6916	71.1146
Ecolomb	46.4474	61.8649
Kinetic	157.7533	220.1111
Total Cp	372.4876	531.0293
Total Energy	372.491	531.0356
pV	0.006160	0.008847
Total + pV	372.4972	531.0445

The constant pressure heat capacity (Cp) was calculated from the temperature dependence of the average energy components obtained from molecular dynamics (MD) simulations. Simulations were performed at a series of temperatures, and the average values of various energy terms (e.g., bond, angle, dihedral, van der Waals, Coulombic, kinetic, and total energy) were extracted.

For each energy component, the variation with respect to temperature was analyzed by performing a linear regression of the form:

$$E(T) = aT + b \quad \textbf{(S21)}$$

where E(T) is the average energy at temperature T, a is the slope (representing dE/dT), and b is the intercept. The slope a provides the contribution of that energy component to the heat capacity:

$$Cp\_component = dE/dT \quad \textbf{(S22)}$$

The total heat capacity was obtained by summing the contributions from relevant components, excluding potential energy (to avoid double-counting terms already present in

bonded and non-bonded interactions), as follows:

$$Cp\_total = Cp\_Bond + Cp\_Angle + Cp\_Dihedral + Cp\_Evdw + Cp\_Ecolomb + Cp\_Kinetic \quad \textbf{(S23)}$$

Additionally, the slope of the total energy and total energy plus pV term was also used to validate the consistency of the Cp calculation. A good linear correlation (high R^2 values) confirmed the reliability of the linear fits.

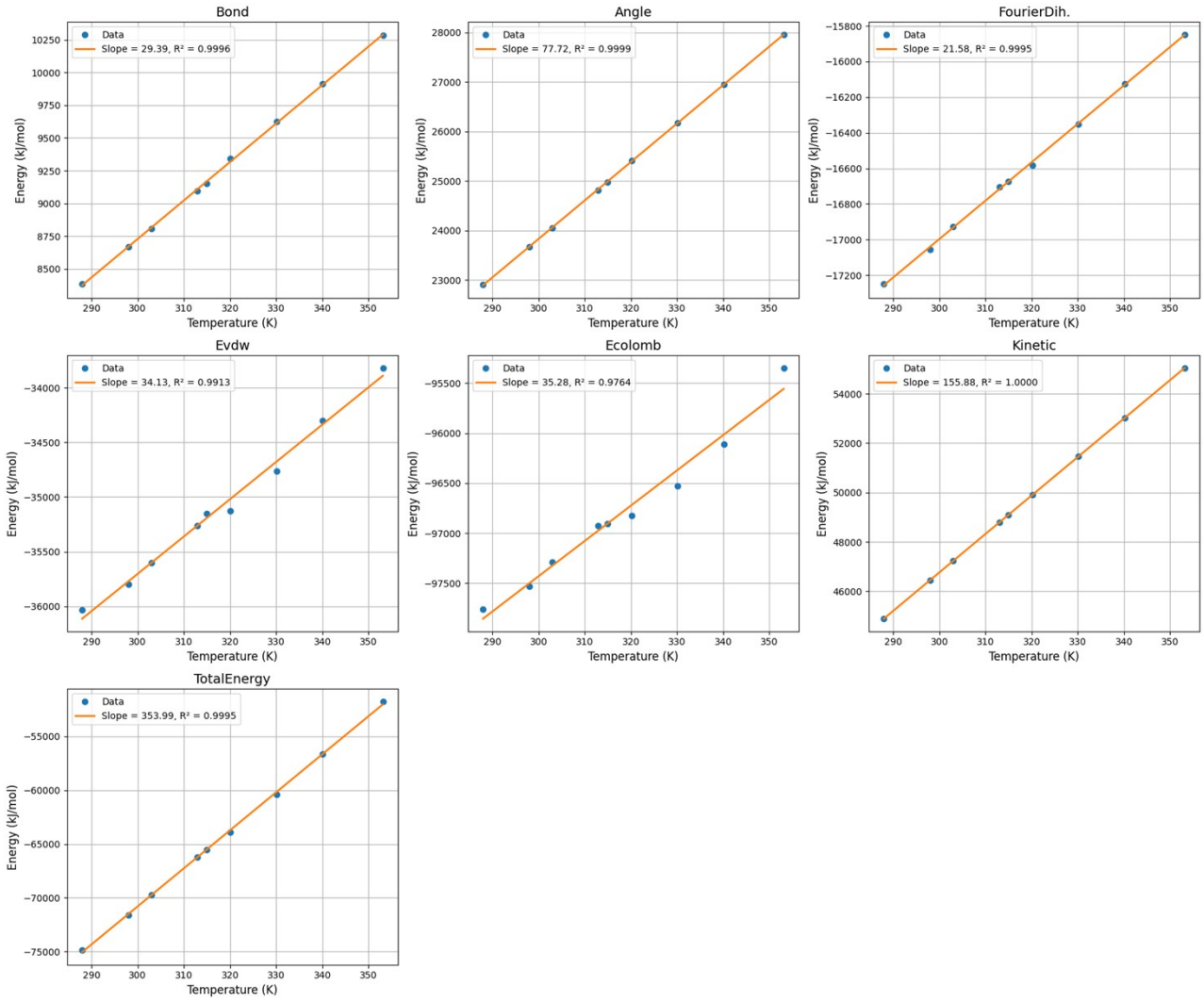

Figure S11. Temperature dependence of internal energy components for the [BMIM][BF4] system obtained from molecular dynamics simulations. The plots show linear fits to energy

vs. temperature for each energy term: bond, angle, Fourier dihedral, van der Waals (Evdw), electrostatic (Ecolomb), kinetic, and total energy. The slopes of the fitted lines correspond to the specific heat capacity (Cp) contributions of each component. R^2 values close to 1 indicate excellent linear correlation, validating the decomposition of Cp into individual energetic contributions

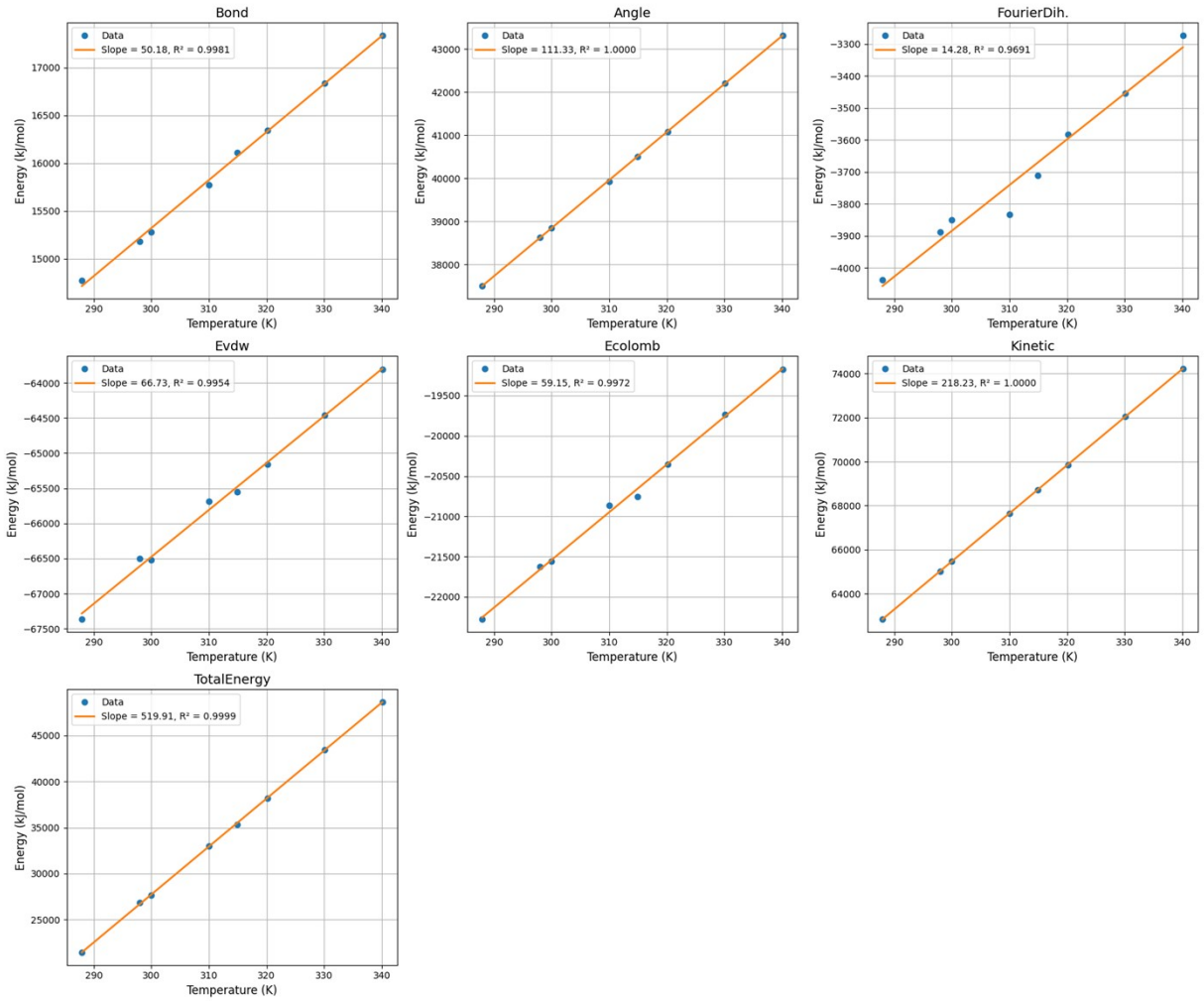

Figure S12. Temperature dependence of internal energy components for the [BMIM][NTF2] system obtained from molecular dynamics simulations. The plots show linear fits to energy vs. temperature for each energy term: bond, angle, Fourier dihedral, van der Waals (Evdw), electrostatic (Ecolomb), kinetic, and total energy. The slopes of the fitted lines correspond to the specific heat capacity (Cp) contributions of each component. R^2 values close to 1 indicate

excellent linear correlation, validating the decomposition of Cp into individual energetic contributions

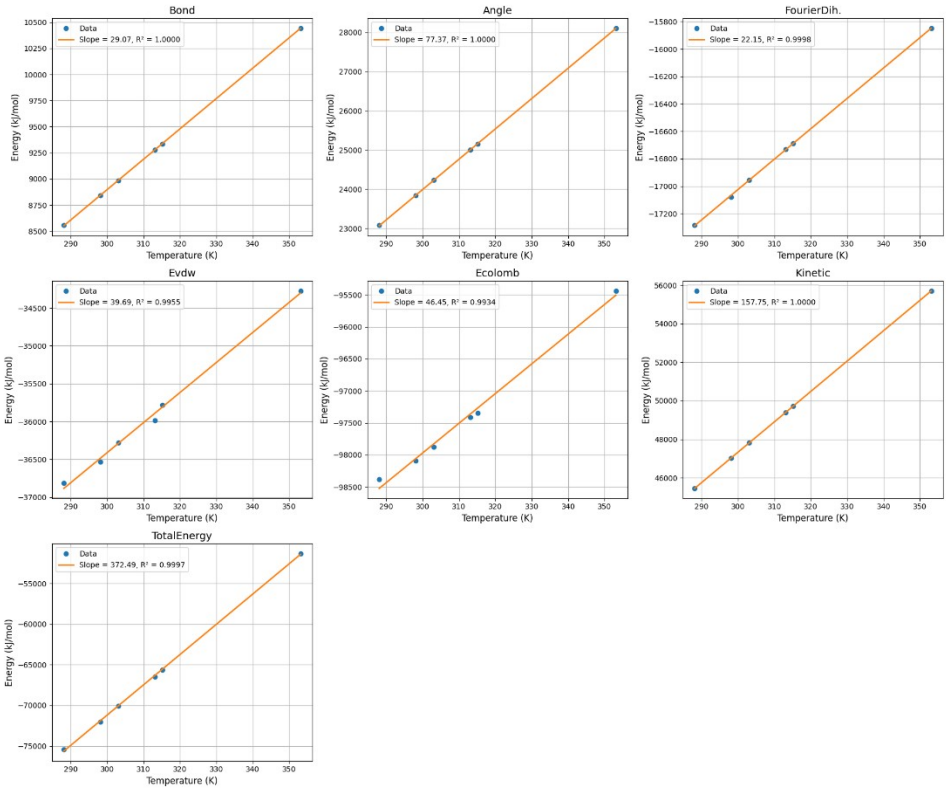

Figure S13. Temperature dependence of internal energy components for the [BMIM][BF4] + CO_2 system obtained from molecular dynamics simulations. The plots show linear fits to energy vs. temperature for each energy term: bond, angle, Fourier dihedral, van der Waals (Evdw), electrostatic (Ecolomb), kinetic, and total energy. The slopes of the fitted lines correspond to the specific heat capacity (Cp) contributions of each component. R^2 values close to 1 indicate excellent linear correlation, validating the decomposition of Cp into individual energetic contributions

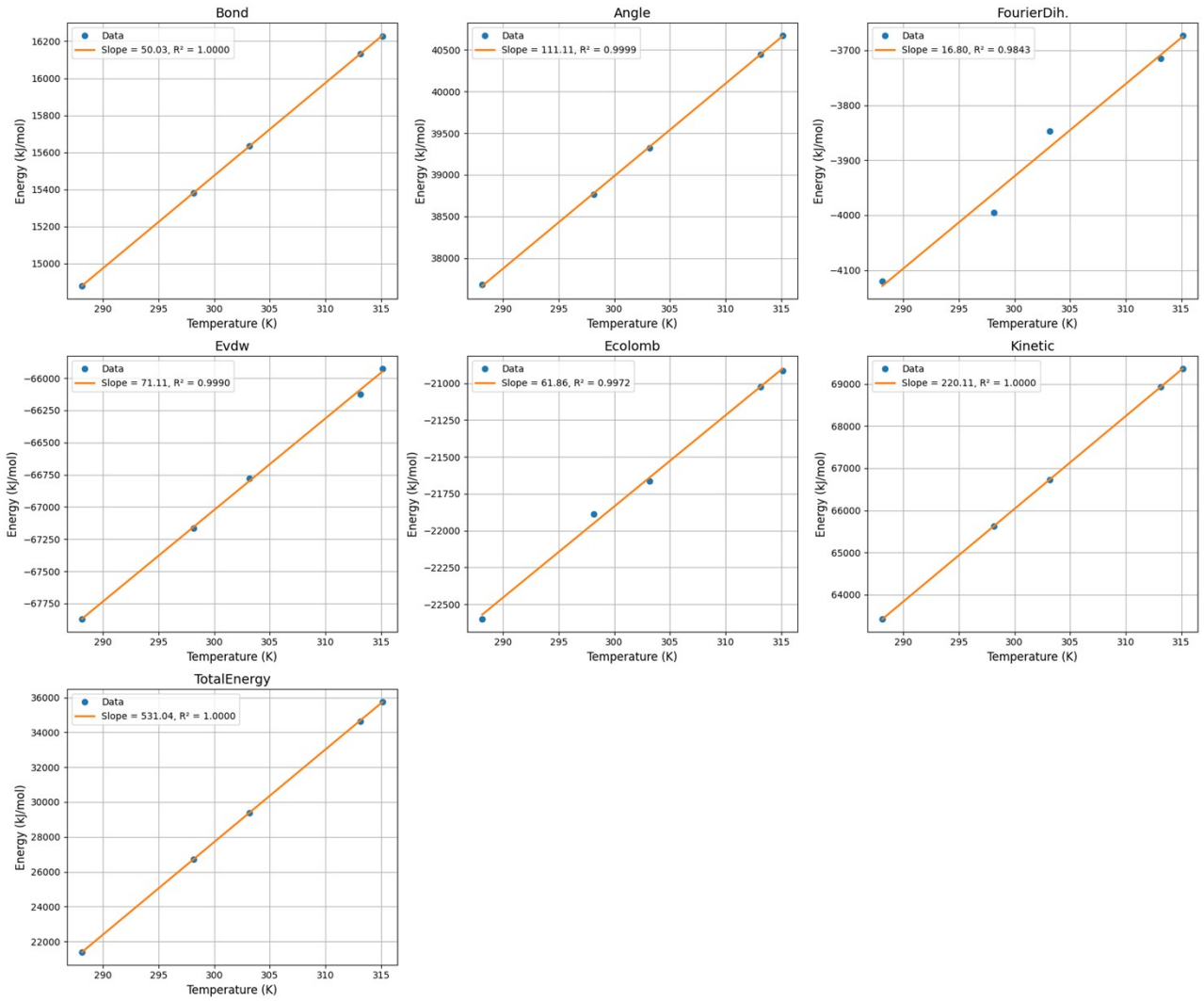

Figure S14. Temperature dependence of internal energy components for the [BMIM][NTF2] + CO_2 system obtained from molecular dynamics simulations. The plots show linear fits to energy vs. temperature for each energy term: bond, angle, Fourier dihedral, van der Waals (Evdw), electrostatic (Ecolomb), kinetic, and total energy. The slopes of the fitted lines correspond to the specific heat capacity (Cp) contributions of each component. R^2 values close to 1 indicate excellent linear correlation, validating the decomposition of Cp into individual energetic contributions

Using the heats of dissolution **(Table 3)** and the pure-IL heat capacities **(Table 4),** of **Main Manuscript** an approximate regeneration energy for each system can be estimated as the sum of the dissolution enthalpy and the sensible heat required to heat the solvent over a 50 K temperature swing: A temperature increase of **50 K** was selected because it corresponds to a realistic operating temperature swing used in many IL-based absorption–desorption cycles (typically from ~303 K during absorption to ~353 K during regeneration). Using this ΔT = 50 K, the sensible heat contribution was calculated from CpΔT, where Cp is the heat capacity of the pure ionic liquid : $q_{reg} \approx |\Delta H| + \frac{C_p \Delta T}{1000}$, ΔH is in kJmol-1.C_p in J.mol^{-1}.K^{-1}.ΔT in K,

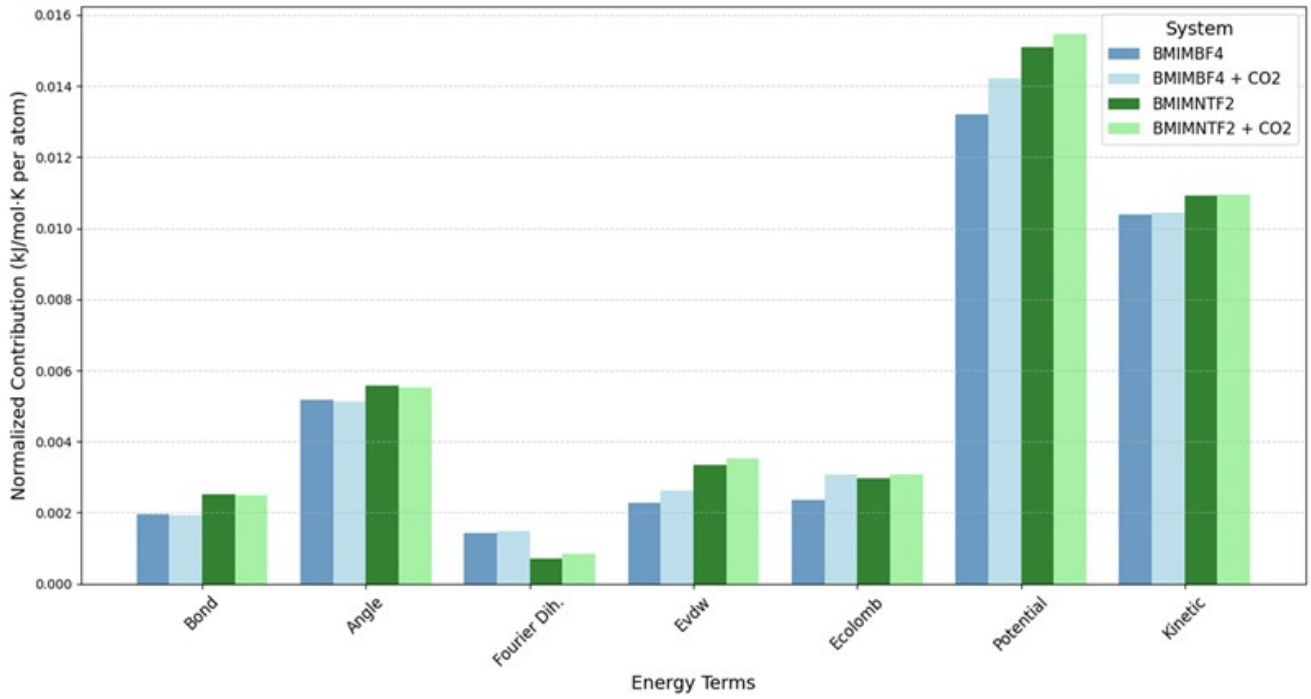

Figure S15. Normalized energy contributions per atom for [BMIM][BF4] and [BMIM][NTF2], with and without CO_2. Energy terms include bonded (bond, angle, Fourier dihedral), non-bonded (Lennard-Jones or van der Waals, electrostatic), potential, and kinetic components.

S9. Estimation of Surface Tension

The method of Irving and Kirkwood (IK) [29, 30] expresses the surface tension through the z dependent local components of the pressure tensor. The surface tension γ_{lv} was determined from the using equation (6). To do so, the rectangular box of $L_x = L_y = 50$ Å and $L_z = 150$ Å dimension with desired ion pairs was used. Equilibration runs under NVT conditions for 10 ns were employed at 300 K, and another 10 ns was performed to calculate the average surface tension. Long-range electrostatic interactions accounted for using the particle-particle particle-mesh solver with a cut-off of 12 Å and accuracy of $1.0e^{-4}$. It is crucial to note that the thickness of the film needs to be enough large to avert system size effects.

$$\gamma_{lv} = \frac{L_z}{2}\left[\langle P_T(Z)\rangle - \langle P_N(Z)\rangle\right] \qquad (S24)$$

where L_z is the box length, $P_N(Z) = P_{ZZ}(Z)$ normal and $P_T(Z) = (P_{xx}(Z) + P_{yy}(Z))/2$ tangential components of the pressure tensor.

Among the two ILs, [BMIM][BF4] exhibits a higher surface tension than [BMIM][NTF2], which can be attributed to its more compact interfacial structure and stronger cohesive interactions. [BMIM][BF4] exhibits higher surface tension than [BMIM][NTF2], primarily due to the smaller size, higher symmetry, and stronger Columbic interactions of the [BF4] anion. These characteristics promote tighter ionic packing and reduced mobility at the liquid interface. In contrast, the larger and more flexible [NTF2] anion, with its fluorinated groups and delocalized charge, disrupts interfacial ordering and creates a more fluid-like interface, leading to lower surface tension. The sharper interface and higher peak density of [BMIM][BF4] indicate stronger interfacial ordering compared to [BMIM][NTF2].

Table16. Surface tension (γ)values for pure ILs and CO_2/ILs. For uncertainty quantification, the data were divided into five equal-length blocks (2 ns per block), and the average surface tension was computed for each. The overall mean was taken as the final value, and the standard deviation across these five blocks was reported to represent the statistical error.

System	(mN/m)	
	Literature	Our study
[BMIM][BF4]	44.4[28] 58.9[1]	58.59 ± 4.25
[BMIM][NTF2]	42.78[31] 30.0 (21)[28]	40.58 ± 3.67

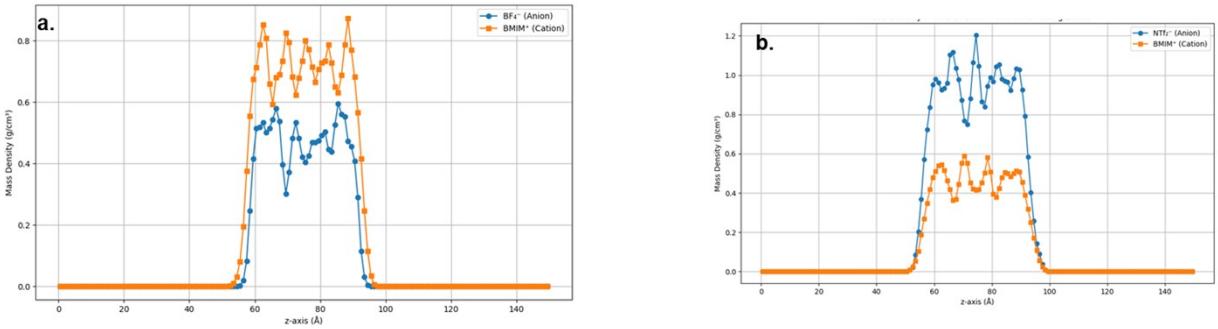

Figure S16. Mass density profiles along the z-axis for the IL/vacuum and IL/CO_2 interfaces. (a) [BMIM][BF4] and (b) [BMIM][NTF2] in pure IL systems

REFERENCES

1. M. Aghaie, N. Rezaei and S. Zendehboudi, *Journal of Molecular Liquids*, 2020, **317**, 113497.
2. R. Hamidova, I. Kul, J. Safarov, A. Shahverdiyev and E. Hassel, *Brazilian Journal of Chemical Engineering*, 2015, **32**, 303-316.
3. J. Jacquemin, P. Nancarrow, D. W. Rooney, M. F. Costa Gomes, P. Husson, V. Majer, A. A. Pádua and C. Hardacre, *Journal of Chemical & Engineering Data*, 2008, **53**, 2133-2143.
4. D. Frenkel and B. Smit, *Understanding molecular simulation: from algorithms to applications*, Elsevier2023.
5. S. Jost, P. Biswas, A. Schüring, J. Kärger, P. A. Bopp, R. Haberlandt and S. Fritzsche, *The Journal of Physical Chemistry C*, 2007, **111**, 14707-14712.
6. M. B. Shiflett and A. Yokozeki, *Industrial & Engineering Chemistry Research*, 2005, **44**, 4453-4464.
7. T. Umecky, Y. Saito and H. Matsumoto, *The Journal of Physical Chemistry B*, 2009, **113**, 8466-8468.

8. S. Duluard, J. Grondin, J. L. Bruneel, I. Pianet, A. Grélard, G. Campet, M. H. Delville and J. C. Lassègues, *Journal of Raman Spectroscopy: An International Journal for Original Work in all Aspects of Raman Spectroscopy, Including Higher Order Processes, and also Brillouin and Rayleigh Scattering*, 2008, **39**, 627-632.
9. M. Y. Yang, B. V. Merinov, S. V. Zybin, W. A. Goddard III, E. K. Mok, H. J. Hah, H. E. Han, Y. C. Choi and S. H. Kim, *Electrochemical Science Advances*, 2022, **2**, e2100007.
10. Y. Hou and R. E. Baltus, *Industrial & Engineering Chemistry Research*, 2007, **46**, 8166-8175.
11. M. S. Green, *The Journal of chemical physics*, 1954, **22**, 398-413.
12. M. S. Green, *The Journal of Chemical Physics*, 1952, **20**, 1281-1295.
13. A. P. Thompson, H. M. Aktulga, R. Berger, D. S. Bolintineanu, W. M. Brown, P. S. Crozier, P. J. In't Veld, A. Kohlmeyer, S. G. Moore and T. D. Nguyen, *Computer physics communications*, 2022, **271**, 108171.
14. K. Goloviznina, Z. Gong and A. A. Padua, *Wiley Interdisciplinary Reviews: Computational Molecular Science*, 2022, **12**, e1572.
15. B. A. Luty and W. F. van Gunsteren, *The Journal of Physical Chemistry*, 1996, **100**, 2581-2587.
16. L. Martínez, R. Andrade, E. G. Birgin and J. M. Martínez, *Journal of computational chemistry*, 2009, **30**, 2157-2164.
17. J. Kang and L.-W. Wang, *Physical Review B*, 2017, **96**, 020302.
18. Q. Zhou, L.-S. Wang and H.-P. Chen, *Journal of Chemical & Engineering Data*, 2006, **51**, 905-908.
19. B. Doherty, X. Zhong, S. Gathiaka, B. Li and O. Acevedo, *Journal of chemical theory and computation*, 2017, **13**, 6131-6145.
20. M. Vranes, S. Dozic, V. Djeric and S. Gadzuric, *Journal of Chemical & Engineering Data*, 2012, **57**, 1072-1077.
21. J. J. Potoff and J. I. Siepmann, *AIChE journal*, 2001, **47**, 1676-1682.
22. B. L. Eggimann, Y. Sun, R. F. DeJaco, R. Singh, M. Ahsan, T. R. Josephson and J. I. Siepmann, *Journal of Chemical & Engineering Data*, 2019, **65**, 1330-1344.
23. L. Hong, J. Lin, D. Gao and D. Zheng, *Scientific Reports*, 2024, **14**, 7586.
24. U. Kapoor and J. K. Shah, *The Journal of Physical Chemistry B*, 2018, **122**, 9763-9774.
25. M. E. Perez-Blanco and E. J. Maginn, *The Journal of Physical Chemistry B*, 2010, **114**, 11827-11837.
26. W. Shi and E. J. Maginn, *The Journal of Physical Chemistry B*, 2008, **112**, 2045-2055.
27. S. Li, W. Zhao, G. Feng and P. T. Cummings, *Langmuir*, 2015, **31**, 2447-2454.
28. M. E. Perez-Blanco and E. J. Maginn, *The Journal of Physical Chemistry B*, 2011, **115**, 10488-10499.
29. J. H. Irving and J. G. Kirkwood, *The Journal of Chemical Physics*, 1950, **18**, 817-829.
30. J. Z. Yang, X. Wu and X. Li, *The Journal of chemical physics*, 2012, **137**, 134104.
31. M. Vraneš, A. Tot, S. Papovic, N. Zec, S. Dozic and S. Gadzuric, 2014.